ChemPhysChem

Research Article
doi.org/10.1002/cphc.202400832

Chemistry Europe
European Chemical Societies Publishing

www.chemphyschem.org

Electrochemical and Thermal Evolution of P2 $Na_{2/3}MnO_2$

B. D. K. K. Thilakarathna,*[a] Uttam Mittal,[a] Jian Peng,[a] Daniel Brocklebank,[a] Helen E. A. Brand,[b] and Neeraj Sharma*[a]

P2 $Na_{2/3}MnO_2$ can be used as a cathode material in sodium-ion batteries. Here, the electrochemical-temperature-dependent evolution of P2 $Na_{2/3}MnO_2$ is investigated using X-ray powder diffraction. P2 $Na_{2/3}MnO_2$ powder under a N_2 atmosphere shows evidence of the formation of a monoclinic *C*2/*m* phase, from about 450 °C. The P2 $Na_{2/3}MnO_2$ electrode sealed in a capillary undergoes a sequence of phase transitions from the as-prepared hexagonal $P6_3/mmc$ to a secondary hexagonal $P6_3/mmc$ phase followed by a transition to Mn_3O_4 and subsequently MnO. NaF also appears parallel to the formation of the secondary hexagonal phase. These transitions suggest a local reducing environment as the Mn oxidation state evolves from $3^+/4^+$ to 2^+. The samples at various states of charge show similar thermal evolution with the exception of the discharged (Na-inserted) state which features a slightly more complex evolution. Understanding the structure and thermal evolution at various states of charge and under various conditions provides insight into the stability of these potential cathode materials.

Introduction

Lithium-ion batteries (LIB) are currently one of the most widely used rechargeable batteries due to their ability to store high amounts of energy.[1] Their high energy density makes them attractive for various applications, from grid-scale energy storage systems to hybrid and electric vehicles to small-scale mobile electronic devices.[2] However, growing concerns about safety, environmental impact, production cost, and scalability have prompted scientists to look for alternative candidates to overcome these limitations.[1] Therefore, in recent years, significant attention has been directed towards developing new battery chemistries and materials that can offer better performance and safety while being cost-effective and environmentally sustainable.[3–5]

Sodium-ion batteries (NIBs) have emerged as a promising alternative due to the high abundance of sodium in the Earth's crust, which makes them potentially cost-effective.[6] NIBs also show a relatively high redox potential, Na^+/Na with $E^\circ = -2.71$ V relative to the standard hydrogen electrode, which is only slightly lower than that of lithium, Li^+/Li with $E^\circ = -3.04$ V.[7] However, the lower energy density of NIBs remains a major challenge for certain applications.[8] To address key challenges and enhance other essential parameters for improved performance, battery components need to be developed and optimised, for example, energy-dense electrodes that permit safe operation.[9]

In this regard, the development of efficient and safe cathode materials is critical for the performance and safety of NIBs.[3,5] Various materials have been explored as potential cathode materials, including layered transition metal oxides, phosphates,[10] NASICON's,[11] sodium transition metal fluorophosphates,[12] and Prussian blue analogs.[13] The choice of cathode material largely depends on the application's specific requirements, such as energy density, power density, and stability.[3] For example, layered transition metal oxides have been extensively studied as cathode materials due to their high energy density.[5,14] They also offer good theoretical capacity and demonstrate high conductivity and fast diffusion kinetics, but in some cases, they suffer from poor cycle stability, which can limit their practical application.[3,15] The continual development and fundamental understanding of processes occurring in these cathode materials will allow for better cathode design.[16]

Layered transition metal oxides, Na_xTMO_2, where *TM* is one or more transition metals[14,17] are classified based on the environment surrounding the sodium ions and the *TM* oxide layers, which features edge sharing octahedra and specific stacking sequences.[15] For these layered compounds, there are two main classifications, O-type where the Na^+ sits in an octahedrally coordinated environment and P-type where the Na^+ sits in a prismatic environment. A number is included in the classification which refers to the number of *TM* oxide layers in the unit cell and this leads to the major phases that are often reported such as P2, P3, O2, and O3.[17,15]

In particular, sodium manganese oxides are an attractive electrode material due to their high energy density, for example, β-$NaMnO_2$ delivers 190 mA h g^{-1} at a rate of C/20,[18] and the abundance of manganese in the Earth's crust.[19] The phase formed typically depends on the Na/Mn ratio.[6] The O3 structure has a sodium stoichiometry of approximately 1, while

[a] B. D. K. K. Thilakarathna, U. Mittal, J. Peng, D. Brocklebank, N. Sharma
School of Chemistry, UNSW, 2052 Sydney, NSW, Australia
E-mail: b.thilakarathna@unsw.edu.au
neeraj.sharma@unsw.edu.au

[b] H. E. A. Brand
Australian Synchrotron, Australian Nuclear Science and Technology Organisation, 800 Blackburn Road, ClaytonVictoria 3168, Australia

Supporting information for this article is available on the WWW under https://doi.org/10.1002/cphc.202400832

in the P2 structure, the sodium stoichiometry typically ranges from 0.5 to 0.75.[20] Even though O3 $NaMnO_2$ can show a high initial capacity (185 $mAhg^{-1}$),[21] its reversible capacity abruptly decreases from the second cycle onwards predominantly because of the substantial structural changes as a result of the extraction of sodium.[22] P2 $Na_{2/3}MnO_2$ can deliver 175 mAg^{-1} during its first discharge and typically exhibits better cycling performance and rate-capability than the O3 phases.[23] The observed capacity of these compounds varies depending on the current rate and precise composition. Focusing on the P2 phases, they can also undergo phase transitions during cycling, which can impact electrochemical performance, e.g., reduce the capacity retention. One significant factor contributing to these phase transitions is the Jahn-Teller distortion of the Mn^{3+} ion. The redox reaction of Mn^{3+}/Mn^{4+} with Na^+ insertion/extraction causes changes in the MnO_6 and hence the structure which can lead to adverse impacts on the material's performance.[6] As a result, researchers have focused on substitutional modifications to P2 $Na_{2/3}MnO_2$, such as replacing Mn with one or more metals, to shift the initial Mn ion oxidation state closer to +4.[17,24]

It is important to note that the phase that is formed can also be tailored by the synthesis procedure. Table 1 summarizes some of the reported annealing temperatures and methods that have been used for the synthesis of different phases of $Na_{2/3}MnO_2$. For instance, using Na_2CO_3 and Mn_2O_3 with heating to 1050 °C followed by rapid quenching was shown to stabilize the orthorhombic P'2 phase (can be considered as a distorted P2 phase) while annealing at 700 °C followed by slow cooling to 500 °C and subsequent quenching stabilizes the P2 phase, a hexagonal phase.[6] Interestingly, it was also noted that the phase formation differed based on the cooling rate, even when the annealing temperature and precursors remained constant. For instance, annealing at 900 °C followed by slow cooling favored the formation of the P2 phase, whereas quenching promoted the formation of the P'2 phase.[5] This example highlights the sensitivity of the resulting structure to the specific synthesis conditions. Moreover, the synthesis procedure's intricacies can lead to the emergence of a residual O'3 (monoclinic) phase due to sodium loss during the heating process.[5] This aspect underscores the multifaceted factors of the synthesis procedures that influence the final material composition and structure.

Table 1. Selected synthesis details of P2 $Na_{2/3}MnO_2$ and related phases.

Phase and space group	Method	Annealing temperature	Ref.
Hexagonal (*P6$_3$/mmc*) + around 20% residual monoclinic (*C2/m*)	Solid state, slow cooled.	900 °C	[5]
Orthorhombic (*Cmcm*) + around 30% residual monoclinic (*C2/m*)	Solid state, quenched	900 °C	[5]
Orthorhombic (*Cmcm*) + an impurity	Solid state	1050 °C	[6]
Hexagonal (*P6$_3$/mmc*)	Solid state	700 °C	[6]
Hexagonal (*P6$_3$/mmc*) + residual orthorhombic (*Cmcm*)	Solid state	600 °C	[25]
Hexagonal (*P6$_3$/mmc*) + orthorhombic (*Cmcm*) in a 55:45 ratio	Solid state	1000 °C	[14]
Hexagonal (*P6$_3$/mmc*)	Solid state	900 °C	[26]
Hexagonal (*P6$_3$/mmc*)	Solid state	900 °C	[24]
Predominantly hexagonal (*P6$_3$/mmc*)	Solid state	900 °C	[27]
Orthorhombic (*Cmcm*)	Hydro-thermal	900 °C	[33]
Hexagonal (*P6$_3$/mmc*) + about 30% orthorhombic (*Cmcm*) + an impurity	Sol-gel	900 °C	[29]
Predominantly hexagonal (*P6$_3$/mmc*)	Sol-gel	850 °C	[30]
Predominantly hexagonal (*P6$_3$/mmc*)	Co-precipitation	720 °C	[31]
Predominantly hexagonal (*P6$_3$/mmc*)	Ultra-Sonication, Spray Pyrolysis	800 °C	[32]

The solid-state method has been the most reported route to synthesize the P2 phase, with synthetic temperatures ranging from 600 °C and 1000 °C.[5,6,14,25,26,24,27] Methods such as sol-gel (with a final heating step at 850 °C),[28–30] co-precipitation (with a final heating step at 720 °C),[31] and ultrasonically assisted spray pyrolysis (with a final heating step at 800 °C)[32] have also been employed, see Table 1. Determining an accurate phase composition after synthesis is crucial for a comprehensive understanding of the relationship between electrochemistry and crystallography.[26] While numerous studies utilizing solid-state synthesis at 900 °C have successfully produced the P2 phase with high purity,[26,24,27] some have reported the presence of a residual monoclinic phase at this temperature, accounting for approximately 20% of the phase fraction[5]. Furthermore, investigations into solid-state synthesis revealed a residual orthorhombic phase when annealed at both 1000 °C[14] and 600 °C.[25] Even though P2 $Na_{2/3}MnO_2$ may appear to be a straightforward composition, the flexibility in Na content, loss of Na at high temperatures and variable Mn oxidation state are highly correlated which can lead to the formation of many related structures that in turn require careful characterization.[5]

Several studies have been dedicated to developing models and gaining insights into the thermal behaviour of layered Na_xTMO_2 compounds after synthesis or after electrochemical cycling.[26,34,35] Thermal analysis was conducted on both P2 and O3 Na_xMO_2 (M = Ti, Cr, Mn, Co, Ni) to examine the temperature dependence of lattice parameters to determine the thermal expansion coefficient and the evolution of the oxygen position parameters. Experiments were carried out from room temperature to 800 K showing linear thermal expansion coefficients ranging from 0.48–1.3×10^{-5} K^{-1} and 1.37–2.72×10^{-5} K^{-1} in the *a* and *c* axes respectively. No evidence of phase transitions was noted and the authors constructed a hard sphere model to develop a theoretical model for expansion properties.[34]

A comprehensive study of the thermal properties of layered Na_xVO_2 (ranging from room temperature to 270 °C) was conducted, alongside an investigation into its electrochemical phase evolution within the range of $0.5 \leq x \leq 1$. This study led to the development of an extensive phase diagram. The

findings suggest that the complexity of electrochemical and thermal phase evolution in Na_xVO_2 arises from the ordered arrangement of sodium/vacancy between the metal oxide layers, driven by the relatively large ionic radius of Na ions and the possibility of the metal oxide layer gliding. This work has identified transformations within Na_xVO_2, which can be categorized as either irreversible or reversible. Briefly, the O3-$NaVO_2$ converts into O'3-$Na_{1/2}VO_2$, $Na_{0.55}VO_2$, and O'3-$Na_{2/3}VO_2$ via cell cycling and selected compositions were studied as a function of temperature. Low Na-content materials, O'3-$Na_{1/2}$VO2 and O'3-$Na_{0.55}VO_2$ undergo an O'3→P'3 transition after heating to 200 °C. Further heating up to 270 °C results in a reversible transformation to the P3 structure. However, the Na-rich O'3-$Na_{2/3}VO_2$ does not exhibit any structural changes under the same treatment conditions.[35] Notably, this study yielded novel metastable phases of Na_xVO_2 through sodium electrochemical (de)intercalation at room temperature, phases that were previously inaccessible via conventional synthesis methods. Many works investigate the thermal properties of Na_xTMO_2 using techniques such as thermogravimetric analysis (TGA) or differential scanning calorimetry (DSC). For example, combining XRD with TGA, P2 $Na_{0.67}MnO_2$ was shown to readily exchange Na^+ with H^+ by absorbing moisture from the atmosphere forming hydrated $Na_{0.67}MnO_2$. The TGA experiment on the hydrated P2 $Na_{0.67}MnO_2$ showed dehydration and decomposition of $NaHCO_3$ within the temperature range of 70–130 °C, deprotonation of $Na_{0.67-x}H_xMnO_2$ occurring between 130–217 °C, decomposition of Na_2CO_3 at temperatures above 130 °C, and the recrystallization process of the P2 phase at temperatures exceeding 483 °C. Work on hydrated P2 $Na_{0.67}Zn_{0.1}Mn_{0.9}O_2$ showed differences to hydrated P2 $Na_{0.67}MnO_2$, e.g., the recrystallization temperature of the P2-type $Na_{0.67}Zn_{0.1}Mn_{0.9}O_2$ phase was found to be lower at 376 °C and this was coupled with related work on $Na_{0.67}TM_{0.1}Mn_{0.9}O_2$. This work was trying to show that hydrated $Na_{0.67}MO_2$ samples can be restored to their original structures through high-temperature annealing.[26]

Here, following synthesis, and structural and electrochemical characterization of P2 $Na_{2/3}MnO_2$, its thermal evolution is determined. Furthermore, the thermal evolution of P2 $Na_{2/3}MnO_2$ at various states of charge and discharge, i.e., varying Na content, is determined and the evolution is compared across the series. The phase transitions and their associated weight fractions, and lattice parameter evolution for state of charge and temperature allows us to develop a comprehensive understanding of the electrochemical-thermal phase evolution.

Results and Discussion

The synthesis procedure of P2 $Na_{2/3}MnO_2$ was optimised after experimenting with several different annealing procedures, and the XRD data related to this process are shown in Figure S1. The resulting SEM and EDX data for P2 $Na_{2/3}MnO_2$ are shown in Figure S2 and Table S1. The Rietveld-refined fit of the P2 $Na_{2/3}MnO_2$ structural model to the XRD data is shown in Figure S3 and the refined structural data is presented in Table S2. A minor impurity may be present as evident by the weak shoulder on the 004 and 100 reflections. P2 $Na_{2/3}MnO_2$ adopts $P6_3/mmc$ space group symmetry with refined lattice parameters of $a = 2.864(3)$ and $c = 11.1390(3)$ Å which are similar to those reported by Liu et al.[29] The lattice parameters of some of the previously reported Na_xMnO_2 phases (where $0.5 < x < 0.8$) have been summarized in Table S3 for comparison. The electrochemical performance of a P2 $Na_{2/3}MnO_2$ based half-cell is shown in Figure S4. The initial discharge capacity was 168 $mAhg^{-1}$, which decreased to 123 $mAhg^{-1}$ at the 23rd cycle and then slowly decreased to 72 $mAhg^{-1}$ by the 100th cycle.

The thermal evolution of the as-prepared powder of P2 $Na_{2/3}MnO_2$ under a N_2 atmosphere is shown in Figure 1a. Rietveld analysis revealed that the P2 $Na_{2/3}MnO_2$ phase is present throughout the temperature range up to 750 °C. The lattice parameters and volume expand with temperature. However, the rate of expansion experiences a notable change around 450 °C, which correlates to the emergence of a new phase. Various structural models were used to describe the secondary phase with the best fit being a monoclinic Na_xMnO_2 model with $C2/m$ space group symmetry.[36] Figure 1b shows the Rietveld refined fit of the structural models with XRD data at 450 °C where both phases distinctively co-exist. Figure 1c shows the evolution of 002 and 001 reflections for the hexagonal and monoclinic phases respectively, during the heat treatment. The evolution of the lattice parameters, volume, and weight fractions of both phases are shown in Figure 2 and S5a. The monoclinic $C2/m$ phase gradually increases at the expense of the hexagonal $P6_3/mmc$ phase reaching over 50% by 750 °C. The transition from a hexagonal $P6_3/mmc$ or P2 to a monoclinic $C2/m$ phase with temperature is unusual as most compounds transform from low symmetry to higher symmetry structures with temperature.[25] However, as shown in Table 1 and S3 there appear to be a variety of possible Na_xMnO_2 phases that can form around this composition and within an open N_2 atmosphere, Na-loss and/or slight Mn reduction during thermal treatment cannot be fully discounted. Considering that the monoclinic $C2/m$ phase is often reported as being Na-rich, the mechanism may involve the formation of monoclinic $Na_{\sim 1}MnO_2$ with a correlated loss of Na in the hexagonal phase, i.e., $Na_{2/3-x}MnO_2$. This correlates with a distinct expansion in the c lattice parameter for the hexagonal phase between 400–500 °C (Figure 2), noting that a reduction in the Na concentration results in an expansion of the c lattice parameter due to the increased repulsion from neighbouring O in the TMO_6 layers. It should be noted that at the highest temperatures of 750 °C, a small proportion of Mn_3O_4 can be modelled. Upon cooling to room temperature a combination of hexagonal, monoclinic Na_xMnO_2 and a minute quantity of Mn_3O_4 is observed, see Figure S5b.

Considering the phase evolution of P2 $Na_{2/3}MnO_2$ during electrochemical charge-discharge, Figure S6 shows the points of extraction, Rietveld-refined fits, and phase composition as a function of the state of charge. Figure S7 shows zoomed regions of these fits and Figures S8-S10 show the refined lattice parameters and volume. Note the cycled electrodes were extracted on the 2nd cycle. The electrode remains wholly hexagonal $P6_3/mmc$ or P2 at the partially charged (PC), fully charged (FC), partially discharged (PD) and as expected at the

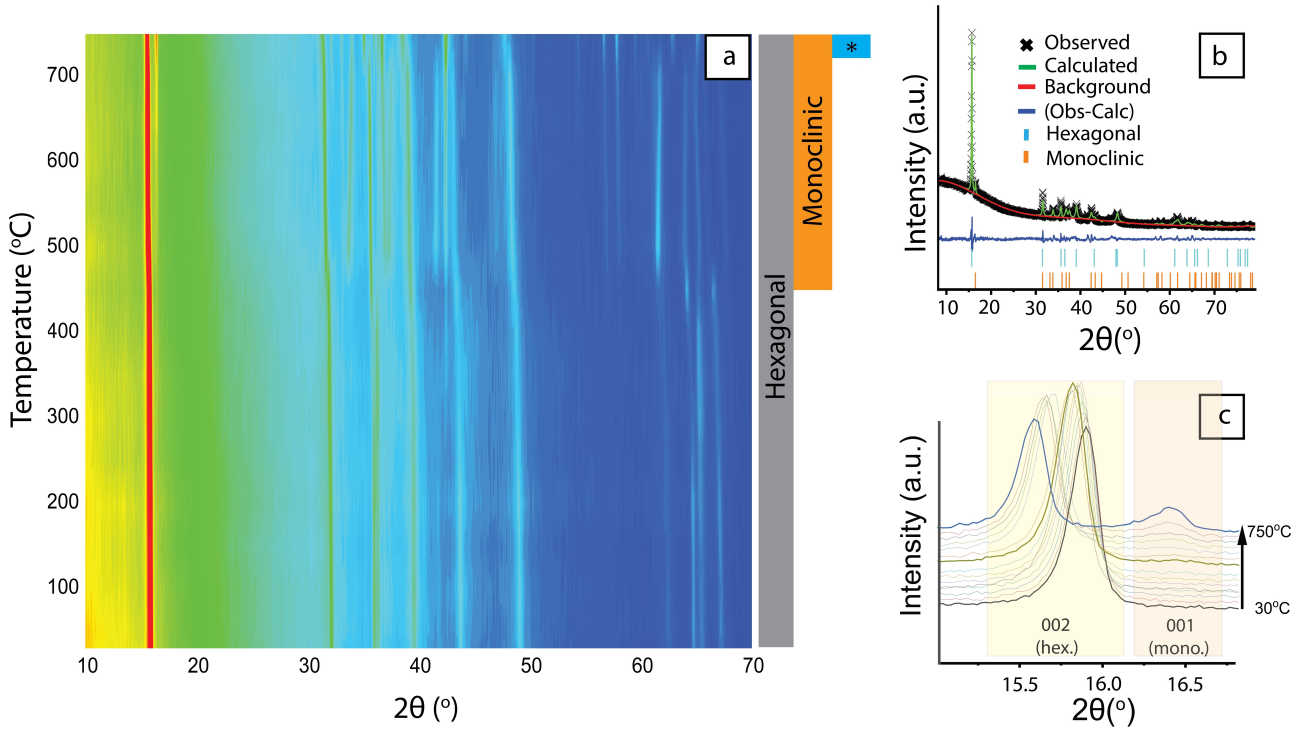

Figure 1. (a) Contour plot of the diffraction data (λ = 1.5418 Å), (b) Rietveld-refined fit at 450°C and (c) zoom of the stacking axes (002) in *P6₃/mmc* and (100) in *C2/m*. The * refers to the Mn_3O_4 phase.

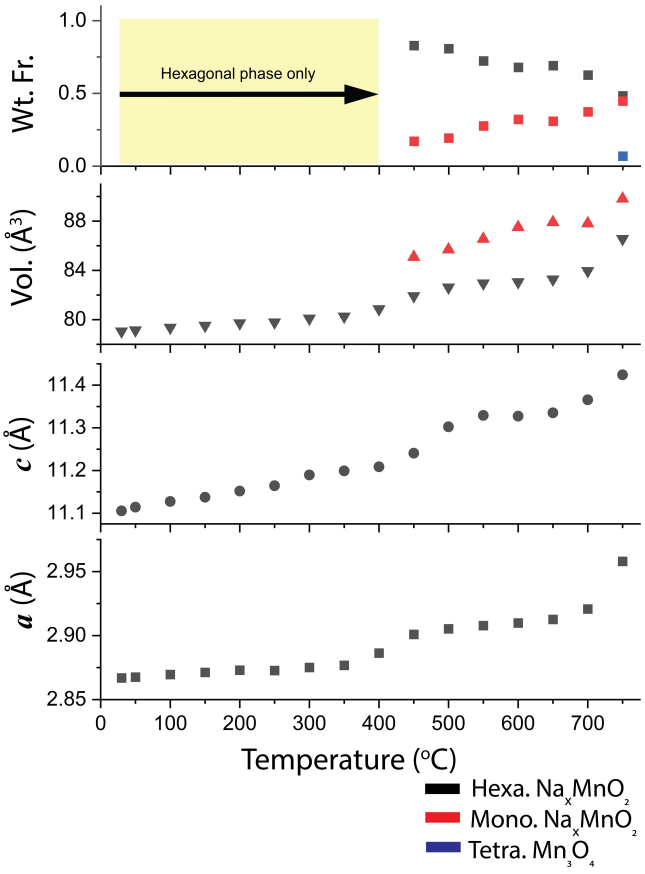

Figure 2. Lattice parameters of the hexagonal *P6₃/mmc* phase, volume and weight fractions of both hexagonal and monoclinic phases as a function of temperature.

non-cycled (NC) sample. At the discharged states where Na is fully inserted, there are more phases present. In the 1st discharged state (FD) a monoclinic phase was found to coexist with orthorhombic phases and at the 2nd discharged state (FD_R) orthorhombic, hexagonal *P6₃/mmc* and monoclinic phases co-exist. The transition to an orthorhombic *Cmcm* phase during the discharging process from the hexagonal *P6₃/mmc* phase has been reported previously.[6]

It is worthwhile to compare this evolution with the evolution found in the literature, Table S3 shows selected studies with the phases reported and where possible lattice parameters and Na content noted. The evolution of volume and lattice parameters of all phases derived from this study are shown in Table S4. The observed hexagonal *P6₃/mmc* or P2 lattice parameters of the NC, PC, FC and PD samples closely align with those reported in the literature.[5,6,14] Interestingly, the hexagonal *P6₃/mmc* phase is not observed in sample FD.

Figure S8 shows that the hexagonal *P6₃/mmc* phase volume of the NC sample is comparatively higher than the FC electrode; however, it is lower than PC and PD samples. The highest volume is shown by sample FD_R among all analysed samples. A similar trend was observed in *a* lattice parameter evolution while the *c* lattice parameter shows the opposite behaviour. The *c* lattice parameter is related to the interplanar distance between the transition metal oxide layers.[6,37] The NC sample shows a comparatively lower *c* lattice parameter compared to the FC sample and this correlates with the literature.[6] As Na is removed from the lattice, there is significant O–O interaction between the transition metal oxide layers which results in an expansion of the *c* lattice parameter. The NC *c* lattice parameter

is larger than the PC and PD electrodes likely indicating a larger amount of Na in the electrodes. The smallest *c* lattice parameter is observed in the FD_R electrode which correlates to the highest Na content. Overall, at the higher Na content states a contraction of the *c* lattice parameter was observed.

At the discharge states, the presence of multiple phases are clearly noted and this posed a challenge for phase identification. Distinguishing the most probable phase among the variety of phases required careful analysis. Therefore, various structural models and combinations of structural models were explored to determine or estimate the most probable structures. Based on the combination of visual fitting, i.e., peak mis-match, and statistical results from Rietveld analysis, as shown in Tables S5 and S6, the structural models that best fit the data are used at these states. Note, that a similar approach was applied during the thermal analysis (discussed below).

The FD_R electrode is of interest as there is a mixture of phases and the hexagonal *P6₃/mmc* phase shows the largest volume (3.0% larger than the NC) and smallest *c* lattice parameter (1.8% smaller than the NC). This is likely the most Na-rich hexagonal *P6₃/mmc* phase in this work. Note, previous work shows an 11.2% volume change between $x = 0.327$ and 0.998 in Na_xMnO_2.[38] The reported lattice parameters for the orthorhombic *Cmcm* phase[29] and the monoclinic *C2/m* phase[36] are similar to the corresponding parameters observed in samples FD and FD_R. Note, the differing Na content in these phases may account for some differences in the lattice parameters. In the literature, the commonly reported phase at the higher Na content, e.g., from $x = 0.74$ to 0.96,[29] is orthorhombic *Cmcm* or P'2 based on XRD[6,24,29,39] and NMR[29] studies. The occurrence of the orthorhombic phase was also documented at $x < 0.67$[6] and $x < 0.715$[38] in some work. The differences in the volume of the orthorhombic *Cmcm* phases at the discharged states was only 0.16%.

There is a variety of reported phase transitions during electrochemical cycling for nominally P2 $Na_{2/3}MnO_2$. In an *in situ* study of P2 Na_xMnO_2 five distinct hexagonal phases all adopting *P6₃/mmc* could be identified during the cycling process.[14] NMR work probing the ^{23}Na chemical shift suggests the presence of a monoclinic phase during the discharge step between $0.45 < x < 0.68$ and in the 2nd charge cycle between $0.76 < x < 0.55$ and this is supported by XRD studies.[29] Samples FD and FD_R appear to exhibit a monoclinic *C2/m* phase with weight fractions of 0.16(1) and 0.24(1), respectively. The monoclinic phase lattice parameters are higher in the FD_R sample compared to the FD sample (Figure S10).

Therefore, the overall phase evolution at room temperature appears to show orthorhombic *Cmcm* and monoclinic *C2/m* at FD first discharge, hexagonal *P6₃/mmc* phase at PC, FC and PD stages, and then a combination of hexagonal *P6₃/mmc*, orthorhombic *Cmcm*, and monoclinic *C2/m* in the FD_R stage (Figure S9).

It is interesting to understand and compare the thermal evolution of the samples extracted at various states of charge and the as-synthesized powder. Figure 3 shows the phase evolution as a function of temperature and state of charge. These were determined using sequential Rietveld analysis with various structural models. Each phase was modelled using a range of different potential structures and the model with the best fit is presented. These experiments are conducted in a quartz capillary with a static Ar atmosphere. It should be noted that all electrodes contain polyvinylidene fluoride (PVDF) and carbon black, and previous work has shown that PVDF melts around 450 °C[40] see TGA data in Figure S12 of ref.[41] Work has also shown the impact of binder on the thermal evolution on active materials. Furthermore, it should be noted that the electrodes are composites, during electrochemical processes surface layers do form and during electrode extraction, washing and drying, salts derived from the electrolyte can remain on the electrodes. Considering the quantity of these components and their crystallinity, in a diffraction pattern the crystalline active material signal dominates. Therefore, the thermal evolution is a complex interaction of these species where the crystalline component from the active material dominates as does its evolution. The sequence of reactions are impacted by the components, e.g., the melting of PVDF or the reaction with carbon black and potential formation of reductive gases such as CO_2.

For these refinements, the background, weight fraction and lattice parameters were refined. The profile parameters were kept constant wherever possible. For each phase, crystal size and strain terms were determined from a single refinement and subsequently fixed. Atomic parameters were kept at the values reported in the Inorganic Crystal Structure Database (ICSD)[42] as the complexity in the phases present didn't allow sufficient reliability to refine these parameters.

One of the key challenges in this work was identifying the phases around 200–350 °C in each case and phases below 350 °C for the discharged sample. In order to identify the phases present, e.g., monoclinic, hexagonal, orthorhombic, temperatures were selected which featured the highest weight fraction of each phase. For example, in the NC sample at 400 °C the phase termed 'secondary' had the highest intensity. This phase was initially modelled with a secondary P2 (hexagonal, *P6₃/mmc*)[29] or P'2 (orthorhombic, *Cmcm*) phase, in addition to the original P2 phase and NaF and Mn_3O_4 present at this temperature. The phases for Na_xMnO_2 were typically found in the ICSD and are shown in Tables 1 and S3. Inspecting the quality of the refinements, *i.e.*, peak matching, and statistics of the fit, either the hexagonal or the orthorhombic phase obtained good quality fits, see Table S8. Sequential refinements were typically undertaken using both structural models, however, the cases presented here were on the best-fit model. In some cases, clear peaks can be identified for certain structural models.

Figure 3a shows that very similar phases are formed across the electrochemical series as a function of temperature with the presence of a secondary hexagonal *P6₃/mmc* (except in FD), NaF, Mn_3O_4 and MnO observed in all cases. In Figure 4b, the contour plots depict the evolution of the (002) reflection for the hexagonal phases, and the (001) reflection for the monoclinic phase between 30 °C and 500 °C. All samples transform into tetragonal Mn_3O_4 followed by cubic MnO and a persistent NaF phase is formed in conjunction. This implies that the environment is reducing as the Mn oxidation state evolves from a mix

Research Article
doi.org/10.1002/cphc.202400832

Chemistry Europe
European Chemical Societies Publishing

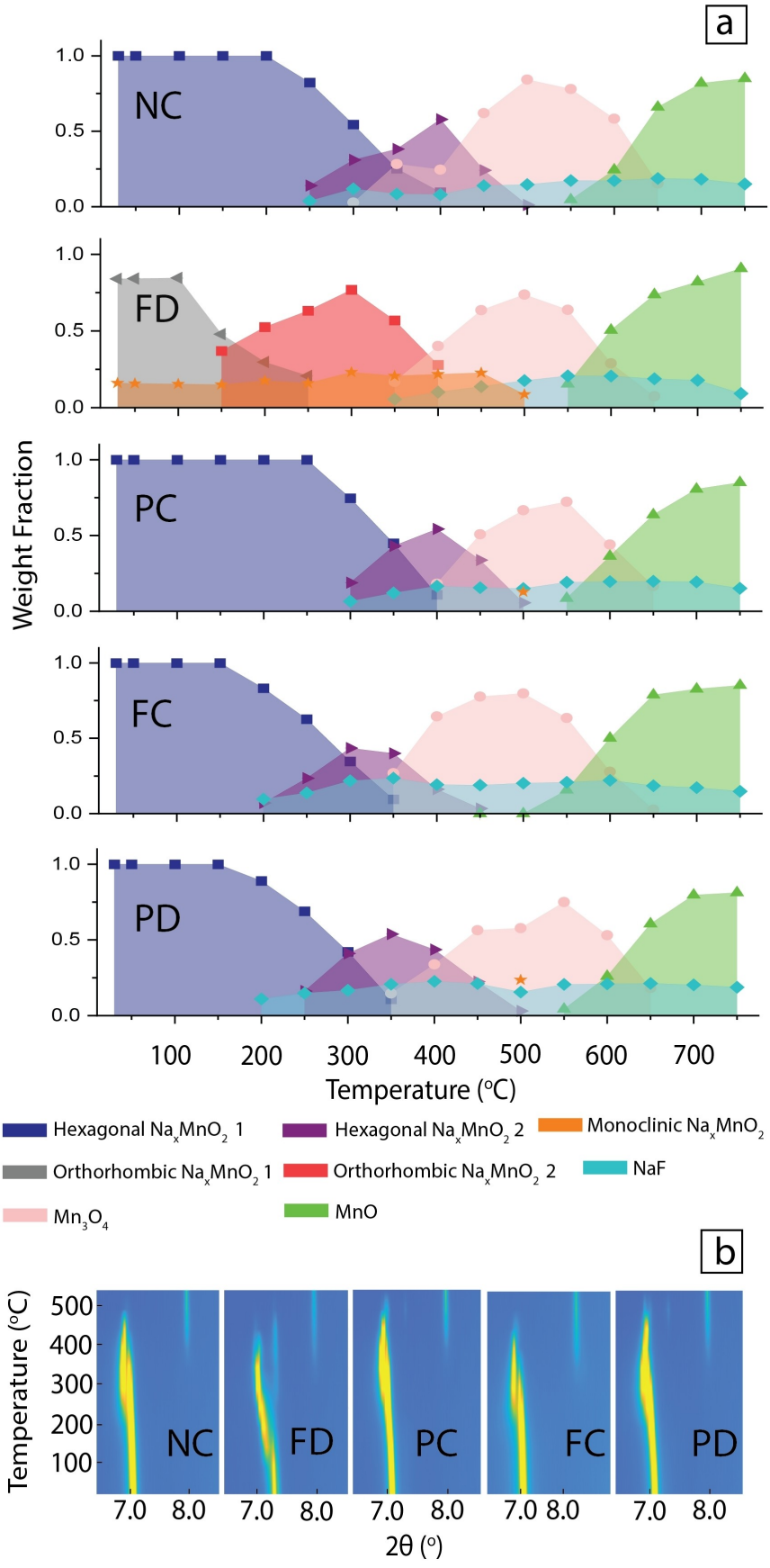

Figure 3. (a) Thermal evolution of Na_xMnO_2 at various states of charge. Weight fractions are derived from Rietveld analysis using a variety of structural models. (b) The contour plots show the evolution of a selected 2θ range (λ = 0.68729(1) Å).

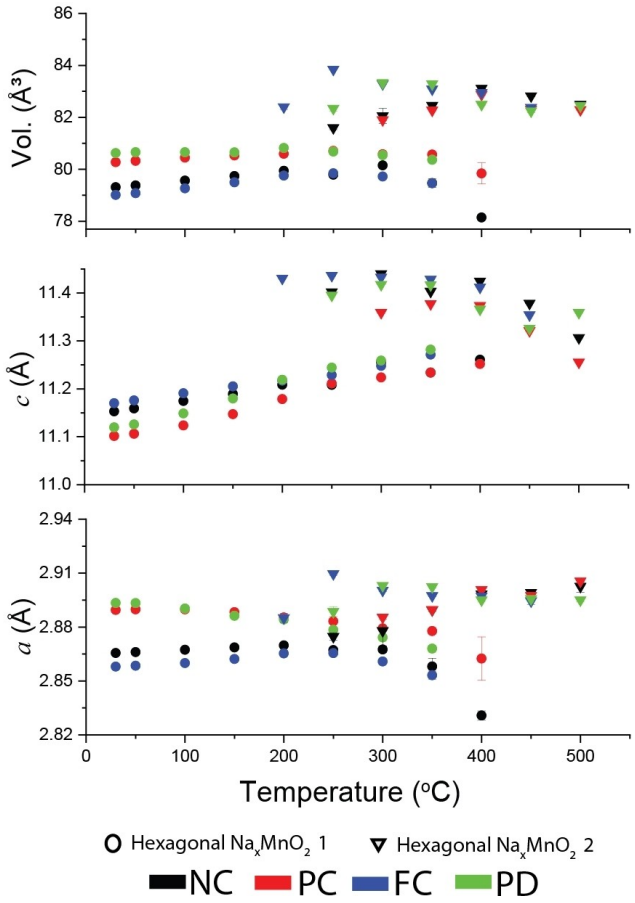

Figure 4. Lattice parameters and volume evolution of the two hexagonal P6$_3$/*mmc* phases found between 30–500 °C.

of $Mn^{3+/4+}$ in the electrodes to $2^+/3^+$ in Mn_3O_4 and 2^+ in MnO. This could be a result of the carbon components and potentially the formation of reducing gases such as CO_2 with thermal treatments.

The PC and PD states of charge are expected to have similar sodium concentrations and show similar phase compositions to the NC electrode. These and the charged (Na-poor) FC electrode show the same phase transitions, from the hexagonal *P6$_3$/mmc* P2 Na_xMnO_2 to a secondary hexagonal *P6$_3$/mmc* P2 Na_xMnO_2 and NaF followed by Mn_3O_4 and MnO. PD and PC show an additional phase, monoclinic *C2/m* O'3 Na_xMnO_2 around 500 °C (shown as a star symbol in Figure 3a). The onset of these transitions and the stability range of the phases vary depending on the state of charge.

In the case of FD or the discharged state (Na-rich), this begins as orthorhombic *Cmcm* P'2 Na_xMnO_2 at room temperature with a residual amount of monoclinic *C2/m* O'3 Na_xMnO_2 (see Figure S11), then transforms to a secondary orthorhombic *Cmcm* P'2 Na_xMnO_2 phase with temperature. As an example, a statistical comparison is shown in Table S8, aiming to establish whether the secondary phase was orthorhombic *Cmcm* or hexagonal *P6$_3$/mmc* at 150 °C. This then transforms to tetragonal Mn_3O_4, cubic NaF and cubic MnO with further heating. Typically, there is a much more complex sequence of phase transitions, especially at lower temperatures, in this Na-rich sample compared to the other lower Na-content state samples.

Furthermore, the formation of the secondary hexagonal *P6$_3$/mmc* phase in the FC sample occurs at a much lower temperature than the formation of the secondary hexagonal *P6$_3$/mmc* phase in other samples. Overall, it is interesting to note that the states of charge or Na-content in the Na_xMnO_2 electrode do not have a large impact on the thermal phase evolution as the secondary Na_xMnO_2 (either hexagonal or orthorhombic), NaF, Mn_3O_4 and MnO are formed in every case probed here. Selected Rietveld refinements of structural models to the XRD data that depict the thermal evolution of each sample are shown in Figure S13.

The original hexagonal *P6$_3$/mmc* to secondary hexagonal *P6$_3$/mmc* Na_xMnO_2 transition is observed at 200 °C for FC, 250 °C for NC and PD and 300 °C for PC. The secondary hexagonal phase becomes the predominant phase between 300 °C to 350 °C for FC, 350 °C to 400 °C for NC, PC and 300 °C to 400 °C for PD. Tetragonal Mn_3O_4 first emerges at 350 °C in NC, FC and PD and 400 °C in PC and becomes the predominant phase between 450 °C and 600 °C in NC, PC and PD and 400 °C to 550 °C in FC. In all samples cubic MnO is clearly observed at 550 °C and tetragonal Mn_3O_4 disappears after 650 °C. In FD, the monoclinic *C2/m* remains until 500 °C, the secondary orthorhombic *Cmcm* forms at 150 °C and dominates between 200 °C and 350 °C and higher temperature evolution follows the other samples. NaF appears between 200–350 °C in all cases.

The lattice parameter and volume evolution as a function of the state of charge and temperature were evaluated. Figure 4 shows the lattice parameter evolution of both hexagonal *P6$_3$/mmc* Na_xMnO_2 phases (in NC, PC, FC and PD). The original hexagonal *P6$_3$/mmc* Na_xMnO_2 *c* lattice parameters overall increase, while the *a* lattice parameter increases to 200 °C for NC and FC and decreases for PC and PD. After 200 °C the *a* lattice parameter decreases for all samples. The volume also shows a change around 200 °C, with an increase in volume below this temperature and a decrease above it in all cases. Note at higher temperatures the errors become larger as the weight fraction of this phase decreases.

The change in the *a* lattice parameter and volume around 200 °C can be caused by a number of factors including the inherent thermal expansion/contraction of this phase, the onset of a phase transition, e.g., formation of the secondary hexagonal *P6$_3$/mmc* phase, and/or a change in the sodium concentration of this phase. Typically, during electrochemical discharge, sodium extraction, from P2-type materials, results in an expansion of the *c* lattice parameter (O–O repulsion from adjacent TMO_6 layers) and a contraction of the *a* lattice parameter (increase in TM oxidation state, reducing *TM*-O bond lengths). The observed thermal evolution particularly after 200 °C is reminiscent of this behaviour, particularly in the primary hexagonal phase.

The secondary hexagonal *P6$_3$/mmc* phase is found between 200–500 °C. Similar lattice parameters are observed across these samples, e.g., at 400 °C, suggesting that similar compositions and structures are being formed in each case. The secondary hexagonal phase shows a general decrease in the *c* lattice

parameters and relatively stable *a* lattice parameters and overall volume. FD was noted earlier to feature a more complex phase evolution than the other samples. The orthorhombic *Cmcm* phase (Figure 5) that is present at room temperature, shows an increase in the *b* and *c* lattice parameters and volume and a decrease in the *a* lattice parameter, and disappears around 250 °C. The secondary orthorhombic *Cmcm* phase that appears at 150 °C shows an initial decrease in the *a* and *b* lattice parameters and volume and an increase in the *c* lattice parameter. After 250 °C, when the original *Cmcm* phase disappears, the *b* lattice parameter and volume begin to increase while *a* remains relatively stable and *c* goes through a maximum and begins to decrease. Furthermore, in FD a small but persistent monoclinic *C2/m* phase could be modelled from room temperature to 500 °C, with only small variations in lattice parameters and volume (Figure S11). In all the samples the cubic *Fm*-3 *m* NaF phase (Figure S12) appears between 200 °C–350 °C and shows linear expansion after 500 °C with a coefficient of thermal expansion of $8.72(1)\times10^{-5}$ K^{-1}.

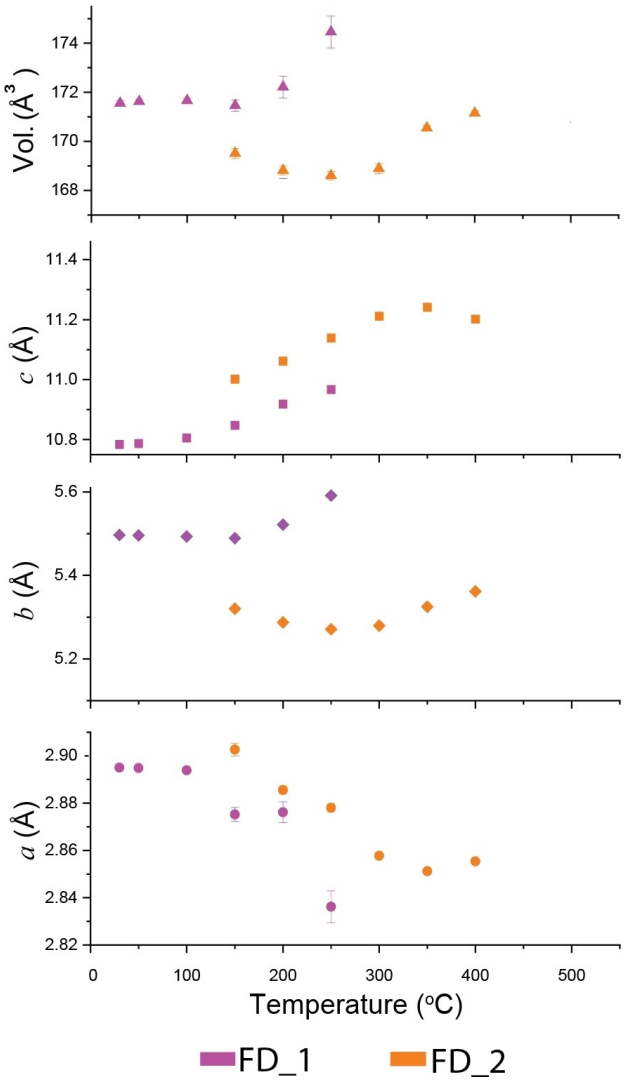

Figure 5. Lattice parameters and volume evolution of the orthorhombic *Cmcm* phase(s), labelled FD_1 and FD_2 found between 30–400 °C in sample FD.

Speculatively, the formation of the NaF can be attributed to the melting of PVDF around 450 °C and reaction of F with Na from Na_xMnO_2, most likely reacting or leaching from the surface of the Na_xMnO_2 particles. This in turn generates Na-deficient regions which transform to MnO_x. The carbon from the carbon black component generates the reducing conditions necessary to drive the reaction to Mn^{4+}. Alternatively, NaF can be present in the cathode electrolyte interphase (CEI) after electrochemical processes and remain on the electrode surface as nanosized components.[43] These components can growth, removing Na and F from the Na_xMnO_2 and PVDF, respectively which in turn results in the formation of MnO_x. It should be noted that the experiments were undertaken in a sealed quartz capillary where the capillary was sealed in an Ar environment, which is slightly reducing.

The occurrence of NaF at relatively low temperatures in the non-cycled electrode suggests a reaction between the binder (PVDF) and Na from Na_xMnO_2. Moreover, in the cycled extracted electrodes the NaF may crystallise from the CEI, i.e., a component in the CEI, or derive from a reaction with any residual electrolyte salts on the electrode or react with the binder. The correlation between NaF formation and the reduction in weight fraction of the original hexagonal *P6$_3$/mmc* phase also provides evidence for such a reaction. Finally, the secondary hexagonal *P6$_3$/mmc* phases noted in all the samples (with the exception of FD) exhibit a larger *c* lattice parameter than the original hexagonal *P6$_3$/mmc* phase, consistent with a smaller concentration of Na in the Na layers of the P2 type Na_xMnO_2 structure.

Figure 6 shows the lattice and volume evolution of the tetragonal Mn_3O_4 and cubic MnO phases. At 350 and 400 °C, Mn_3O_4 appears to show a small spread in the lattice parameters and volume depending on the state of charge. The difference may indicate a small solid solution where Na is present in the structure. However, it should be noted that at 350 °C in particular, the weight fraction of Mn_3O_4 are quite low and this is evident in the larger error bars on the lattice parameters. Overall, Mn_3O_4 and MnO_2 are consistently formed across the samples and similar to NaF from 450 °C show relatively linear thermal expansion. The thermal expansion coefficient for Mn_3O_4 between 400 to 650 °C is $2.47(8)\times10^{-5}$ K^{-1} and for MnO between 550 to 750 °C is $4.29(2)\times10^{-5}$ K^{-1}. MnO and NaF remain after cooling.

Conclusions

This work shows the electrochemical and thermal evolution of P2 $Na_{2/3}MnO_2$ electrodes. P2 $Na_{2/3}MnO_2$ heated under an open N_2 environment forms a secondary monoclinic *C2/m* phase, from about 450 °C and grows to about 52 % at 750 °C. P2 $Na_{2/3}MnO_2$ electrodes, with carbon black and PVDF, and electrochemically cycled variants show very similar high-temperature phase evolution to each other when heated in sealed Ar-filled quartz capillaries. They all transform into NaF, Mn_3O_4 followed

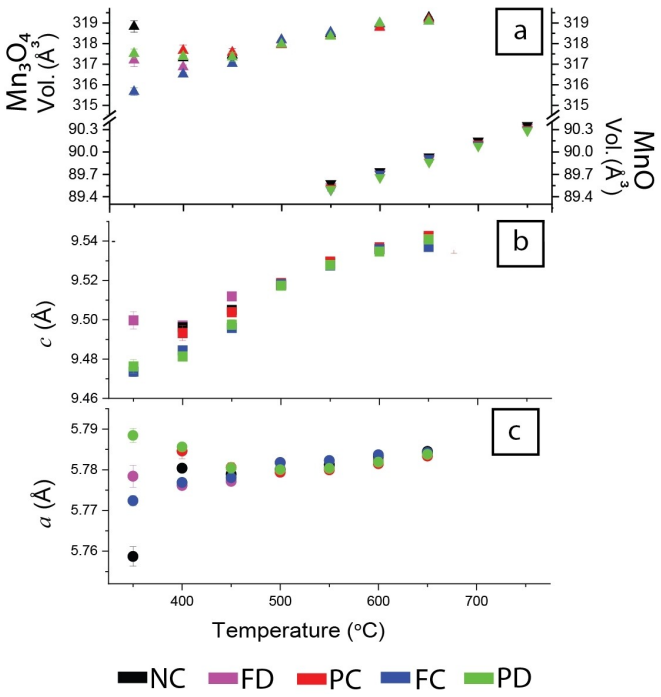

Figure 6. The (a) volume evolution of the Mn_3O_4 and MnO phases and (b-c) the volume and lattice parameter evolution of Mn_3O_4.

by MnO demonstrating a reduction in the Mn oxidation state and a disappearance of crystalline Na-containing layered components. All extracted electrodes, besides the discharged (Na-inserted) state, show an evolution from the original hexagonal *P6₃/mmc* P2 Na_xMnO_2 to a secondary hexagonal *P6₃/mmc* P2 Na_xMnO_2 phases prior to the appearance of Mn_3O_4. The discharged states, show a mix of phases at room temperature, a combination of orthorhombic *Cmcm* and monoclinic *C2/m* at both discharge states and re-emergence of the hexagonal *P6₃/mmc* phase at the 2nd discharge state. The thermal evolution of the first discharged state begins with the orthorhombic *Cmcm* and monoclinic *C2/m* phases, with the monoclinic *C2/m* phase remaining until 500 °C, and the orthorhombic *Cmcm* phase transforming into a second orthorhombic phase around 150 °C before the sample forms NaF and Mn_3O_4. NaF forms between 200-350 °C in all cases. Overall, these results indicate that irrespective of state of charge the thermal phase evolution is very similar under the conditions used. Future work, investigating different external conditions, e.g., evolution under O_2, or with different types of binders may shed light on the stability and accessibility of other phases in this and related systems.

Experimental Section

To synthesize P2 $Na_{2/3}MnO_2$, Na_2CO_3 (Sigma-Aldrich, 99%) and $MnCO_3$ (Fisher, 99%) were ground using a mortar and pestle in a stoichiometric ratio. A Retsch planetary ball mill (400 rpm for 2 hours) was used to further mix the compound. This compound was subsequently calcinated at 650 °C for 15 h, furnace cooled to 530 °C before being quenched to room temperature and stored in an Ar-filled glovebox. Scanning electron microscopy (SEM) and energy-dispersive X-ray spectroscopy (EDS) analyses were conducted using a Hitachi TM4000Plus electron microscope. To identify the phase, laboratory XRD analysis was carried out on a Malvern Panalyical MPD with Cu Kα radiation (λ = 1.5418 Å) and/or Empyrean 2 with Co Kα radiation (λ = 1.7902 Å).

Laboratory variable temperature XRD experiments were performed on as-prepared powders using the Malvern Panalytical Empyrean 1 equipped with a heating stage and Cu Kα radiation (λ = 1.5418 Å). Data were collected at RT, 50 °C, followed by increments of 50 °C to 750 °C with a 50 °C min^{-1} ramp-up rate under a N_2 atmosphere.

Electrodes were prepared by mixing active material (P2 $Na_{2/3}MnO_2$) with carbon black as the conductive agent and polyvinylidene fluoride (PVDF) as the binder in an 80:10:10 weight ratio. The slurry of the mixture was made using N-methyl pyrrolidone (NMP) as the solvent. Next, the mixture was coated onto aluminium foil and dried at 100 °C for 18 h in a vacuum oven. Electrodes of 12 mm diameter were punched out of the coated foil and pressed under a load of 100 kN and dried again before transfer to the glovebox. The electrochemical performance of P2 $Na_{2/3}MnO_2$ was evaluated using coin cells assembled in an Ar-filled glovebox. Metallic sodium was used as the negative electrode and glass fibre separators were used. A solution of 0.6 M $NaPF_6$ in ethylene carbonate, propyl carbonate, and fluoroethylene carbonate (EC/PC/FEC 49:49:2 vol %) was used as the electrolyte.

Galvanostatic cycling for the cells was performed between 4–1.5 V for P2 $Na_{2/3}MnO_2$ on a Landt battery tester. Charge-discharge cycles were typically undertaken with a current density of 20 mAg^{-1} for charge and 10 mAg^{-1} for discharge. To extract the cathodes at different states of charge in their second cycle for thermal studies, the first cycle was conducted with a charging rate of 40 mAg^{-1} and a discharging rate of 10 mAg^{-1}. Subsequently, the second cycle involved a charging rate of 20 mAg^{-1} and a discharging rate of 10 mAg^{-1}. Cells were cycled to achieve fully discharged (1st discharged state), partially charged, fully charged, partially discharged, and another fully discharged state (2nd discharged state). All the cells were cycled at room temperature.

For ex-situ variable temperature synchrotron XRD experiments, the non-cycled and other extracted electrodes from coin cells were washed with dimethyl carbonate (DMC) and dried inside the glovebox. Electrode materials were then scraped from the Al current collector, ground and filled into 0.5 mm quartz capillaries, and sealed inside the glovebox. XRD data were collected on the powder diffraction beamline at the Australian Synchrotron using a wavelength of 0.68729(1) Å. The wavelength was determined by performing Rietveld analysis using XRD data on a NIST LaB_6 reference material collected at the start of the beamtime. Sample data were collected at RT, 50 °C, followed by increments of 50 °C to 750 °C with a 10 °C min^{-1} ramp rate using an FMB Oxford hot air blower. In all cases, two additional data sets were collected during the cooling process at 200 ° C and 30 °C.

Rietveld refinements were carried out using the GSASII software package[44]. Background, profile, weight fractions, lattice and in some cases selected atomic parameters and preferred orientation terms (spherical harmonics) were refined. Various parameters were optimised in a systematic approach and attempts were made to keep parameters consistent across the compositional and thermal series wherever possible.

Acknowledgements

The authors would like to thank the support from our funding programs, Australian Research Council (FT200100707 and DP200100959) and the University International Postgraduate Award (UIPA) from UNSW. Part of this research was undertaken on the powder diffraction beamline at the Australian Synchrotron, part of ANSTO, we acknowledge their technical assistance and the assistance of staff at the Mark Wainwright Analytical Centre (MWAC) at UNSW Sydney. Open Access publishing facilitated by University of New South Wales, as part of the Wiley - University of New South Wales agreement via the Council of Australian University Librarians.

Conflict of Interests

There are no conflicts of interest to declare.

Data Availability Statement

The data that support the findings of this study are available from the corresponding author upon reasonable request.

Keywords: Structural evolution · Sodium-ion batteries · Cathode · Synchrotron X-ray powder diffraction

[1] L. Croguennec, M. R. Palacin, *Chem.I Soc.* **2015**, 3140–3156, https://doi.org/10.1021/ja507828x.
[2] C. Liu, Z. G. Neale, G. Cao, *Materials Today* Elsevier, B. V., 1 March **2016**. 109–123, https://doi.org/10.1016/j.mattod.2015.10.009.
[3] R. J. Clément, P. G. Bruce, C. P. Grey, *J Electrochem Soc* **2015**, *162*(14), A2589–A2604.
[4] N. Yabuuchi, K. Kubota, M. Dahbi, S. Komaba, *Chem. Rev.* **2014**, *114*(23), 11636–11682.
[5] J. Billaud, G. Singh, A. R. Armstrong, E. Gonzalo, V. Roddatis, M. Armand, T. Rojo, P. G. Bruce, *Energy Environ. Sci.* **2014**, *7*, 1387–1391.
[6] S. Kumakura, Y. Tahara, K. Kubota, K. Chihara, S. Komaba, *Angewandte Chemie* **2016**, *128*(41), 12952–12955
[7] Pergamon Texts, Pergamon, in Inorganic Chemistry; Edited by W. A.HartO. F.BeumelT. P.Whaley, **1973**, pp. 331–367, https://doi.org/10.1016/B978-0-08-018799-0.50005-4.
[8] K. M. Abraham, *J Phys. Chem. Lett.* **2015**, 830–844, https://doi.org/10.1021/jz5026273.
[9] J. F. Peters, A. Peña Cruz, M. Weil, *Batteries* **2019**, *5*(1), https://doi.org/10.3390/batteries5010010.
[10] Z. Hao, X. Shi, Z. Yang, X. Zhou, L. Li, C. Ma, S. Chou, *Adv. Mater.* **2023**, https://doi.org/10.1002/adma.202305135.
[11] S. A. Novikova, R. V. Larkovich, A. A. Chekannikov, T. L. Kulova, A. M. Skundin, A. B. Yaroslavtsev, *Inorg. Mater.* **2018**, *54*(8), 794.
[12] S. T. Dacek, W. D. Richards, D. A. Kitchaev, G. Ceder, *Chem. Mater.* **2016**, *28*(15), 5450–5460.
[13] M. He, R. Davis, D. Chartouni, M. Johnson, M. Abplanalp, P. Troendle, R. P. Suetterlin, *J Power Sources* **2022**, 548, https://doi.org/10.1016/j.jpowsour.2022.232036.
[14] D. Sehrawat, A. Rawal, S. Cheong, M. Avdeev, C. D. Ling, J. A. Kimpton, N. Sharma, *Inorg. Chem.* **2020**, *59*(17), 12143–12155.
[15] C. Delmas, C. Fouassier, P. Hagenmuller, *Physica B+C* **1980**, *99*(1), 81–85.
[16] G. Wan, W. Dou, H. Zhu, W. Zhang, T. Liu, L. Wang, J. Lu, *Interdisciplinary Mater.* **2023**, *2*(3), 416–422.
[17] M. H. Han, E. Gonzalo, N. Sharma, J. M. López Del Amo, M. Armand, M. Avdeev, J. J. Saiz Garitaonandia, T. Rojo, *Chem. Mater.* **2016**, *28*(1), 106–116.
[18] J. Billaud, R. J. Clément, A. R. Armstrong, J. Canales-Vázquez, P. Rozier, C. P. Grey, P. G. Bruce, *J Am. Chem. Soc.* **2014**, *136*(49), 17243–17248.
[19] J. M. Studer, W. P. Schweer, N. K. Gabler, J. W. Ross, *Anim. Reprod. Sci.* **2022**, *238*, 106924.
[20] J. H. Stansby, N. Sharma, D. Goonetilleke, *J Mater Chem. A* **2020**, 24833–24867.
[21] X. Ma, H. Chen, G. Ceder, *J Electrochem. Soc.* **2011**, *158*(12), A1307.
[22] M. Palluzzi, L. Silvestri, A. Celeste, M. Tuccillo, A. Latini, S. Brutti, *Crystals (Basel)* **2022**, *12*(7), https://doi.org/10.3390/cryst12070885.
[23] M. A. Khan, D. Han, G. Lee, Y. Il Kim, Y. M. Kang, *J Alloys Compd.* **2019**, *771*, 987–993.
[24] X. Zhang, F. Qiu, K. Jiang, P. He, M. Han, S. Guo, H. Zhou, *Chem. Commun.* **2020**, *56*(46), 6293–6296.
[25] T. Ma, G. L. Xu, X. Zeng, Y. Li, Y. Ren, C. Sun, S. M. Heald, J. Jorne, K. Amine, Z. Chen, *J Power Sources* **2017**, *341*, 114–121.
[26] W. Zuo, J. Qiu, X. Liu, F. Ren, H. Liu, H. He, C. Luo, J. Li, G. F. Ortiz, H. Duan, J. Liu, M. S. Wang, Y. Li, R. Fu, Y. Yang, *Nat Commun.* **2020**, *11*(1), https://doi.org/10.1038/s41467-020-17290-6.
[27] G. Kucinskis, B. Kruze, P. Korde, A. Sarakovskis, A. Viksna, J. Hodakovska, G. Bajars, *Batteries* **2022**, *8*(1), https://doi.org/10.3390/batteries8010006.
[28] K. Hemalatha, M. Jayakumar, P. Bera, A. S. Prakash, *J. Mater. Chem. A* **2015**, *3*(42), 20908–20912.
[29] X. Liu, W. Zuo, B. Zheng, Y. Xiang, K. Zhou, Z. Xiao, P. Shan, J. Shi, Q. Li, G. Zhong, R. Fu, Y. Yang, *Angewandte Chemie* **2019**, *131*(50), 18254–18263.
[30] R. Luo, J. Zheng, Z. Zhou, J. Li, Y. Li, Z. He, *ACS Appl. Mater. Interfaces* **2022**, *14*(42), 47863–47871.
[31] X. Huang, D. Li, H. Huang, X. Jiang, Z. Yang, W. Zhang, *Nano Res.* **2021**, *14*(10), 3531–3537.
[32] C. Luo, A. Langrock, X. Fan, Y. Liang, C. Wang, *J. Mater. Chem. A* **2017**, *5*(34), 18214–18220.
[33] D. Su, C. Wang, H. J. Ahn, G. Wang, *Chem. - A Euro. J* **2013**, *19*(33), 10884–10889.
[34] W. Kobayashi, A. Yanagita, T. Akaba, T. Shimono, D. Tanabe, Y. Moritomo, *Sci. Rep.* **2018**, *8*(1), https://doi.org/10.1038/s41598-018-22279-9.
[35] C. Didier, M. Guignard, M. R. Suchomel, D. Carlier, J. Darriet, C. Delmas, *Chem. Mater.* **2016**, *28*(5), 1462–1471.
[36] J.-P. Parant, R. Olazcuaga, M. Devalette, C. Fouassier, P. Hagenmuller, *J Solid State Chem* **1971**, *3*(1), 1–11.
[37] W. Zuo, X. Liu, J. Qiu, D. Zhang, Z. Xiao, J. Xie, F. Ren, J. Wang, Y. Li, G. F. Ortiz, W. Wen, S. Wu, M. S. Wang, R. Fu, Y. Yang, *Nat Commun* **2021**, *12*(1), https://doi.org/10.1038/s41467-021-25074-9.
[38] C. Wang, L. Liu, S. Zhao, Y. Liu, Y. Yang, H. Yu, S. Lee, G. H. Lee, Y. M. Kang, R. Liu, F. Li, J. Chen, *Nat. Commun.* **2021**, *12*(1), https://doi.org/10.1038/s41467-021-22523-3.
[39] W. Zuo, J. Qiu, X. Liu, B. Zheng, Y. Zhao, J. Li, H. He, K. Zhou, Z. Xiao, Q. Li, G. F. Ortiz, Y. Yang, *Energy Storage Mater.* **2020**, *26*, 503–512.
[40] D. Mouraliraman, N. Shaji, S. Praveen, M. Nanthagopal, C. W. Ho, M. V. Karthik, T. Kim, C. W. Lee, *Nanomaterials* **2022**, *12*(7), https://doi.org/10.3390/nano12071056.
[41] J. Liu, H. L. Andersen, O. K. Al Bahri, S. Bhattacharyya, A. Rawal, H. E. A. Brand, N. Sharma, *Dalton Transactions* **2018**, *47*, 14604–14611.
[42] M. Hellenbrandt, *Crystallography Reviews* **2004**, *10*, 17–22.
[43] X.-F. Guo, Z. Yang, Y.-F. Zhu, X.-H. Liu, X.-X. He, L. Li, Y. Qiao, S.-L. Chou, *Small Methods* **2022**, *6*, 2200209.
[44] B. H. Toby, R. B. Von Dreele, *J Appl. Crystallogr.* **2013**, *46*(2), 544–549.

Manuscript received: August 25, 2024
Revised manuscript received: November 17, 2024
Accepted manuscript online: November 26, 2024
Version of record online: January 28, 2025